


Perfect spin polarization, valley polarization, and tunneling magnetoresistance in bilayer silicene magnetic superlattices

Guangqin Xiong, Tongxin Sun, Yiyi Lou, Tingting Wei,^{*} Xin Li[✉], and Yu Wang^{✉†}

Department of Physics, Faculty of Science, Kunming University of Science and Technology, Kunming 650500, China

 (Received 14 May 2023; revised 27 October 2023; accepted 31 October 2023; published 13 November 2023)

We have theoretically investigated the spin- and valley-dependent transport in the bilayer silicene magnetic superlattices consisting of alternatively ferromagnetic and nonmagnetic domain. The calculation with a four-band scattering matrix method demonstrates that due to the spin- and valley-resolved band splitting in the field-tunable ferromagnetic domains, perfect spin and valley polarization can be engineered for the symmetric superlattice only in its parallel magnetization configuration, while for the asymmetric superlattice, it can be engineered in both the parallel and antiparallel magnetization configurations. For both types of superlattice, a strong contrast in the configuration-dependent conductance makes a field-controllable, yet colossal tunneling magnetoresistance accessible. These features indicate that a bilayer silicene magnetic superlattice might be a potential choice for silicene-based spin-valleytronic applications.

DOI: [10.1103/PhysRevB.108.195414](https://doi.org/10.1103/PhysRevB.108.195414)

I. INTRODUCTION

The experimental synthesis of monolayer and few-layer silicene [1–8] has triggered considerable interest in electronic transport in silicene mesoscopic systems due to its appealing physics [9] and superior compatibility with current integrated technology, the latter of which is highly necessary for the scale fabrication of novel logic devices. Compared to monolayer silicene, better air stability has been experimentally demonstrated for multilayer silicene [10]. This provides a feasible solution to improve the operation time of the silicene field-effect transistor [11] for electronic applications. Thus, in the smallest configuration of multilayer silicene, bilayer silicene (BLS) should be an attractive choice [4,9].

Structurally, BLS can be regarded as two vertically stacked monolayers of silicene in some orders [12]. By means of first-principles calculations, several feasible configurations such as AB-bt [13,14], AA_p [15,16], and slide-2AA [17] have been predicted so far for BLS. Among those configurations, the AB-bt structure is a popular choice due to the possible emergence of exotic properties. For instance, with AB-bt configured BLS, Liu *et al.* theoretically predicted the existence of $d + id'$ chiral superconductivity [13], while Do *et al.* observed the diverse magnetic quantization for the magnetically modulated BLS [18]. Indeed, due to the stronger interlayer covalent interaction, an enhanced intralayer buckling (~ 0.66 Å) [14,17] is well recorded for BLS, being remarkably larger than that for monolayer silicene (~ 0.46 Å). This enhanced buckling further enables BLS to acquire a larger field-tunable band gap and stronger spin-orbit interaction [14], both of which are very beneficial to modulate spin- and valley-polarized transport for silicene-based spin-valleytronic applications.

However, even with the above features, little effort has been given to the spin- and valley-polarized transport in the BLS system [19–21]. In our latest report [22], for a single valley transport, it has been theoretically shown that near perfect spin polarization and its perfect switching are accessible in a field-tunable BLS superlattice. These features enable the BLS superlattice to be a potential candidate for a spin-valley filter application. Unfortunately, for general systems with twofold valley degeneracy, this interesting signal should be canceled in each other due to spin-valley locking. For this reason, to rigorously achieve real spin- and valley-polarized transport in BLS, additional spin- or valley-contrast modulation must be included.

To further break the limitation of spin-valley locking on real spin- or valley-polarized transport in a field-controllable BLS system, making BLS locally magnetic might be a favorable strategy. Previously, it has been shown by Ouyang *et al.* [23] that a fully spin-polarized current can be achieved by making BLS antiferromagnetic, which is an intrinsic property for BLS once its layer distance is larger than 2.6 Å. Unfortunately, for general BLS, the predicted layer distance is only 2.54 Å, indicating the proposed solution might be a challenge. Alternatively, via the magnetic proximity effect, it has been experimentally demonstrated [24–26] that a nonmagnetic film could be ferromagnetic by depositing a ferromagnetic insulating medium atop it. For instance, in the graphene/CrSe heterostructure, the proximity-induced exchange splitting energy in graphene can be up to 134 meV at 2 K [25]. Indeed, for monolayer silicene, several proximity-induced ferromagnetic junctions [27–31] and its arrays [32–37], i.e., a magnetic superlattice (MSL), were theoretically studied. In these structures, both the spin and valley degeneracy of pristine silicene can be fully broken by hybrid magnetic-electric modulation, inducing perfect spin- and valley-resolved transport and pronounced tunneling magnetoresistance (TMR). Inspired by these reports, a ferromagnetic BLS could also be engineered

^{*}weitingting@outlook.com

[†]wyraul107@163.com

by the magnetic proximity effect, but, irrespective of the above attractive properties of BLS, little was acquired on the properties of spin-valley transport in a BLS magnetic superlattice (BLS-MSL).

In this work, to access real spinor-polarized transport in a BLS superlattice without the single-valley approximation required by Ref. [22], by periodically making the silicene ferromagnetic through the array of the surface ferromagnetic electrode [36], spin- and valley-dependent transport have been theoretically investigated for BLS-MSL consisting of alternatively cascaded ferromagnetic and nonmagnetic domains. It is shown that under the periodically magnetic-electric comodulations, fully broken spin-valley degeneracy of local bands forms different periodic potentials for different spinor states, opening a window to observe the permitted transport only for one spinor state but the prohibited scenario for the others. Our calculations indicate that perfect spin and valley polarization are only observed for BLS-MSL having a symmetric, parallel-magnetized unit cell, while for BLS-MSL having an asymmetric unit cell, perfect spin and valley polarization can be accessed for both parallel and antiparallel magnetization configurations. Between both configurations, a strong discrepancy in configuration-dependent conductance leads to the emergence of colossal tunneling magnetoresistance. Importantly, all concerned properties can be effectively tailored by the gate field, which is very suitable for silicene-based spin-valleytronic applications.

The rest of this paper is organized as follows: In Sec. II, we mainly explain the structure of the considered BLS-MSL and our method to calculate the spin- and valley-dependent transport properties. In Sec. III, the calculated properties such as ballistic conductance and tunneling magnetoresistance are, respectively, discussed for BLS-MSL having a symmetric and asymmetric unit cell. We briefly summarize our work in Sec. IV.

II. MODEL AND METHOD

Figure 1(a) schematically depicts our considered BLS-MSL, where a sheet of BLS is assumed to be modulated by top periodically arranged ferromagnetic electrode (FME) pairs (dashed rectangle). In each pair of FMEs, the left subelectrode (FME1) has a width d_L and is laterally separated by L from its right counterpart (FME2), which has a width d_R and is spaced by W from FME1 of the next adjacent FME pair. Due to the magnetic proximity effect, beneath the FMEs, BLS domains could be ferromagnetic with an exchange field $M_L(M_R)$ for the left (right) domain of each FME pair. Here, in order to enable both the parallel and antiparallel magnetization configurations of the ferromagnetic pairs, the right subdomain is assumed to be a softer one, the magnetization of which can be easily reversed by the external magnetic field. As shown in the inset, there are four atoms, namely, A_1 , B_1 , A_2 , and B_2 , in the unit cell of the AB-bt stacked structure, where the B_1 site of the top sublayer is vertically coupled to the A_2 site of the bottom sublayer, while the other site of the top (bottom) sublayer is located in the center of the honeycomb lattice of the bottom (top) sublayer. Due to the buckled lattice, under the modulation of perpendicular electric field F_z , different on-site potentials should be acquired for different sites, thus

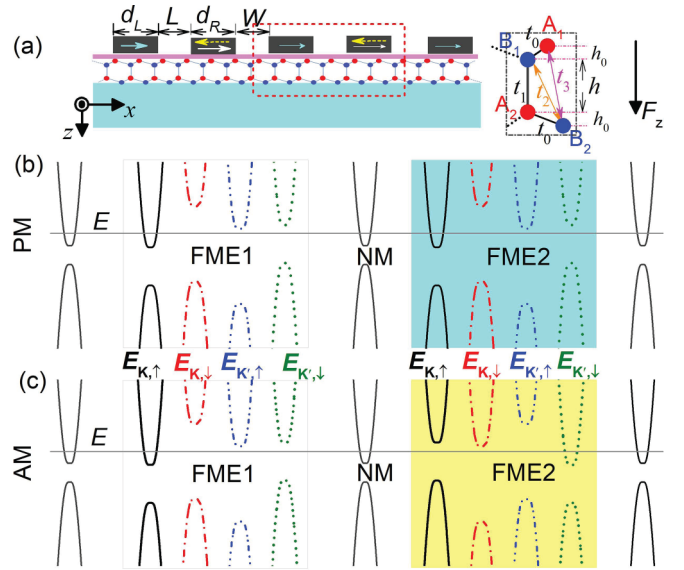


FIG. 1. (a) The schematic plot of symmetric BLS-MSL and the unit cell (inset) of AB-bt stacked BLS. (b), (c) The local band alignments of a periodic unit [the dashed rectangle in (a)] are depicted for two FMEs in their (b) PM and (c) AM configuration with a zero U but a finite Δ_z and M .

endowing BLS a locally field-controllable band gap. Since BLS can be structurally regarded as two coupled monolayers of silicene via proper interlayer interactions, i.e., A_2 - B_1 vertical interaction t_1 , A_2 - A_1 (B_1 - B_2) skew interaction t_2 , and A_1 - B_2 skew interaction t_3 , the electronic properties of BLS near the Dirac points (K and K' valleys) can be modeled by the following low-energy effective Hamiltonian [38,39]:

$$\hat{H} = \begin{bmatrix} U_\sigma + \delta_2 & \hbar v_f k_- & -\hbar v_2 k_- & \hbar v_3 k_+ \\ \hbar v_f k_+ & U_\sigma + \delta_1 & t_1 & -\hbar v_2 k_- \\ -\hbar v_2 k_+ & t_1 & U_\sigma - \delta_1 & \hbar v_f k_- \\ \hbar v_3 k_- & -\hbar v_2 k_+ & \hbar v_f k_+ & U_\sigma - \delta_2 \end{bmatrix}, \quad (1)$$

where $v_{2(3)} = 3a_0 t_{2(3)}/2\hbar$, with a_0 the intralayer Si-Si bond length, and the corresponding basis function taken as $\psi = [\psi_{A_1}, \psi_{B_1}, \psi_{A_2}, \psi_{B_2}]^\dagger$. Previously, to reasonably reproduce the first-principles predicted band structure of BLS, the interlayer tight-binding parameters were suggested as $t_1 = 2.025$ eV, $t_2 = 0.152$ eV, and $t_3 = 0.616$ eV. Thus, considering the smaller strength of t_2 and t_3 in comparison to t_1 , the relating terms have been neglected in this work for simplicity. With this approximation, our model Hamiltonian can be further simplified as

$$\hat{H} = \begin{bmatrix} U_\sigma + \delta_2 & \hbar v_f k_- & 0 & 0 \\ \hbar v_f k_+ & U_\sigma + \delta_1 & t_1 & 0 \\ 0 & t_1 & U_\sigma - \delta_1 & \hbar v_f k_- \\ 0 & 0 & \hbar v_f k_+ & U_\sigma - \delta_2 \end{bmatrix}, \quad (2)$$

with $v_f \approx 0.55 \times 10^6$ m/s the Fermi velocity, \hbar the reduced Planck constant, and $k_\pm = k_x \pm i\eta k_y$, with $k_{x(y)}$ the x (y) component of the two-dimensional momentum and $\eta = \pm 1$ the valley index with plus (minus) for the K (K') valley. $U_\sigma = U + \sigma M$, with $\sigma = \pm 1$ the index with plus or minus for spin-up (\uparrow) or -down (\downarrow) orientation, respectively, U the local electrostatic potential, and M the ferromagnetic exchange

field. Including F_Z and referring to the AB-bt configuration, $\delta_{1(2)}$ in Eq. (1) can be further expressed as

$$\begin{aligned}\delta_1 &= \Delta_Z + \eta\sigma\Delta_{SO}, \\ \delta_2 &= (1 + 2h_0/h)\Delta_Z - \eta\sigma\Delta_{SO},\end{aligned}\quad (3)$$

with the intralayer buckling $h_0 = 0.66 \text{ \AA}$ [17], the vertical A_2 - B_1 separation $h = 2.54 \text{ \AA}$ [17], the intrinsic spin-orbit coupling $\Delta_{SO} = 5 \text{ meV}$ [14], and $\Delta_Z = \hbar F_Z/2$ the field-tunable staggered potential between the A_2 site and B_1 site. Apparently, due to the spin-valley locking, namely, the term $\eta\sigma\Delta_{SO}$, the configuration-dependent transport can not only explicitly depend on the spin index as generally expected for spin-field interaction, but also implicitly depend on the valley index.

Starting from Eq. (2), the resulting eigenvalue equation can be deduced from the condition $|\hat{H} - E| = 0$ as

$$\begin{aligned}[(E - U_\sigma)^2 - \delta_2^2][(E - U_\sigma)^2 - \delta_1^2 - t_1^2] \\ - 2\hbar^2 v_F^2 k^2 [(E - U_\sigma)^2 + \delta_1\delta_2] + \hbar^4 v_F^4 k^4 = 0.\end{aligned}\quad (4)$$

Correspondingly, the explicit energy spectra can be further determined as

$$E = U_\sigma + s\sqrt{\frac{\Gamma + l\sqrt{\Gamma^2 - 4t_1^2\delta_2^2 - 4[(\hbar v_f k)^2 - \delta_1\delta_2]^2}}{2}},\quad (5)$$

with $s = \pm 1$ for the conduction (plus) or valence (minus) band, $l = \pm 1$ for the upper (plus) or lower (minus) band, $k = \sqrt{k_x^2 + k_y^2}$, and $\Gamma = \delta_1^2 + \delta_2^2 + 2(\hbar v_f k)^2 + t_1^2$. From this expression, as can be seen from Figs. 1(b) and 1(c), in the nonmagnetic (NM) domain, i.e., $U = 0$, $M = 0$, and $\Delta_Z = 0$, all spin- and valley-dependent bands are identical and the lowest branch of the conduction bands is separated from the highest branch of the valence bands with a local gap $2\Delta_{SO}$; while for the domain beneath the FME, with a nonzero Δ_Z and M , the calculated bands have been fully split into four spinor-resolved bands, thus opening a finite window to observe fully spin- and valley-polarized transport. By further imposing a nonzero U , the resulting bands would be wholly shifted up and down, forming different band alignments to tailor the transport properties.

For our considered structure, beneath the top gates, a constant U and Δ_Z can be induced by gate-field modulation, whereas it is zero for the NM regions. For M , the resulting distribution can be written as follows:

$$M = \begin{cases} M_L, & (n-1)\Lambda \leq x \leq (n-1)\Lambda + d_L \\ \lambda M_R, & (n-1)\Lambda + d_L + L \leq x \leq n\Lambda - L \\ 0 & \text{otherwise,} \end{cases}\quad (6)$$

with n the integer number for the order of the unit cell from left to right, $\Lambda = W + L + d_L + d_R$ the length of the unit cell, and $\lambda = \pm 1$ denoting the magnetization configuration with plus or minus for parallel magnetization ($\uparrow\uparrow$, PM) or antiparallel magnetization ($\uparrow\downarrow$, AM), respectively. With these potential distributions, both periodic electric and magnetic modulations have been simultaneously achieved in our BLS-MSL, being remarkably different from the recent report for monolayer silicene [36] for which only the periodic magnetic but constant electric modulation is considered.

In a specific region, e.g., the j th domain, due to the interface scattering between neighboring domains, the resulting wave function should be expressed as a superposition of the forward and backward states, which, with a given modulation, could be easily derived from the Schrodinger equation as

$$\psi_j = \sum_{l,\pm} F_{j,\pm}^l \begin{pmatrix} \alpha_{j,\pm}^l \\ 1 \\ \rho_j^l \\ \beta_{j,\pm}^l \end{pmatrix} e^{\pm ik_{j,x}(x-x_{j-1}) + ik_y y},\quad (7)$$

where $F_{j,\pm}^l$ are the unknown coefficients and

$$\alpha_{j,\pm}^l = \frac{\hbar v_f (\pm k_{j,x}^l + i\eta k_y)}{\varepsilon_j - \delta_{1,j}},\quad (7a)$$

$$\beta_{j,\pm}^l = \frac{(\varepsilon_j - \delta_{2,j})\rho_j^l \alpha_{j,\pm}^l}{\varepsilon_j + \delta_{1,j}},\quad (7b)$$

$$\rho_j^l = \frac{\varepsilon_j - \delta_{2,j}}{t_1} - \frac{(\hbar v_f)^2 [(k_{j,x}^l)^2 + k_y^2]}{t_1(\varepsilon_j - \delta_{1,j})},\quad (7c)$$

with \pm for the forward (plus) and backward (minus) states, x_j the location of the j th interface, $\varepsilon_j = E - U_j - \sigma M_j$, and the longitudinal wave vector $k_{j,x}^l$ which can be further derived from Eq. (5) as

$$k_{j,x}^l = \sqrt{\frac{\varepsilon_j^2 + \delta_{1,j}\delta_{2,j} - l\sqrt{\chi}}{\hbar^2 v_f^2} - k_y^2},\quad (8)$$

where $\chi = t_1^2(\varepsilon_j^2 - \delta_{2,j}^2) + \varepsilon_j^2(\delta_{1,j} + \delta_{2,j})^2$.

For the considered modulation, due to the translational invariant along the y direction, k_y should be conserved during electronic tunneling through BLS-MSL from left to right and can be easily derived from the incident lead as

$$k_y = \frac{\sin\theta}{\hbar v_f} \sqrt{E^2 - \Delta_{SO}^2 - l\sqrt{t_1^2(E^2 - \Delta_{SO}^2)}},\quad (9)$$

with θ the carrier incident angle at the left lead.

Evidently, depending on the occupied band, different k_y are expected even for the same θ . By applying the interfacial boundary condition governing wave-function continuity, the final scattering state can be efficiently correlated with the incident state via total scattering matrix $\mathbf{S}(L, R)$, as explained in our previous work [22], which reads

$$\begin{pmatrix} F_{R,+}^- \\ F_{R,+}^+ \\ F_{L,-}^- \\ F_{L,-}^+ \end{pmatrix} = \mathbf{S}(L, R) \begin{pmatrix} F_{L,+}^- \\ F_{L,+}^+ \\ F_{R,-}^- \\ F_{R,-}^+ \end{pmatrix},\quad (10)$$

where the subscript L (R) denotes the left (right) lead, corresponding, respectively, to $j = 0$ and $4n$. Indeed, as can be concluded from Eq. (5), since the energy separation between the upper and lower branches of the conduction bands is of the order of t_1 ($\sim 2.02 \text{ eV}$), only the intraband transport of the lower occupied band has a pronounced contribution for the low-energy electronic transport. This enables the column vector on the right side of Eq. (10) to have the form of $[1, 0, 0, 0]^\dagger$. Thus, the spinor-resolved intraband

transmission probability (T) can be written as

$$T_{\eta,\sigma} = \frac{k_{R,x}^-}{k_{L,x}^-} |S_{11}(L, R)|^2. \quad (11)$$

Following the well-known Landauer-Büttiker formula, under the zero-temperature regime, the corresponding ballistic conductance $G_{\eta,\sigma}$ can be further calculated as

$$G_{\eta,\sigma} = G_0 \int_{-\pi/2}^{\pi/2} T_{\eta,\sigma}(E, \theta) \cos \theta d\theta, \quad (12)$$

where $G_0 = \frac{q^2 L_y}{2\pi^2 \hbar^2 v_f} \sqrt{E^2 - \Delta_{SO}^2 + \sqrt{I_1^2 (E^2 - \Delta_{SO}^2)}}$ is the conductance unit with q the elementary charge and L_y the transverse length of the system.

Correspondingly, for a specific magnetization alignment, the concerned conductance spin (valley) polarization P_S (P_V) can be further expressed as

$$P_S = \frac{G_{K,\uparrow} + G_{K',\uparrow} - G_{K,\downarrow} - G_{K',\downarrow}}{G_{K,\uparrow} + G_{K',\uparrow} + G_{K,\downarrow} + G_{K',\downarrow}} \quad (13)$$

and

$$P_V = \frac{G_{K,\uparrow} + G_{K,\downarrow} - G_{K',\uparrow} - G_{K',\downarrow}}{G_{K,\uparrow} + G_{K',\uparrow} + G_{K,\downarrow} + G_{K',\downarrow}}. \quad (14)$$

To clearly show the configuration-dependent conductance, the modified tunneling magnetoresistance (m-TMR) is also calculated from the following expression:

$$\text{m-TMR} = \frac{G^{\uparrow\uparrow} - G^{\uparrow\downarrow}}{G^{\uparrow\uparrow} + G^{\uparrow\downarrow}}, \quad (15)$$

where $G^{\uparrow\uparrow}$ ($G^{\uparrow\downarrow}$), namely, the denominator of Eqs. (13) and (14), is the total conductance for the PM (AM) configuration. By removing $G^{\uparrow\uparrow}$ from the denominator of Eq. (15), the expression is then reduced to the conventional definition of TMR.

III. RESULTS AND DISCUSSION

In this section, spin- and valley-resolved transport is explicitly demonstrated for two types of BLS-MSL. One is symmetric MSL, for which the unit cell is structurally symmetric, e.g., $d_L = d_R$ and $L = W$, while the other is asymmetric with $d_L \neq d_R$ and $L \neq W$. For both configurations, the invariant parameters are $E = 3\Delta_{SO}$, $n = 10$, $U = 0$, $M = 0.6\Delta_{SO}$, and $\Lambda = 50$ nm.

A. BLS-MSL with symmetric unit cell

The physics for the achievement of spin- and valley-resolved transport in BLS-MSL could be simply understood with its local band alignments. As depicted in Fig. 1(b), within the domain covered by FME, due to the hybrid magnetic-electric modulation, spin- and valley-relying band splitting induces a different modulation for different spinor states. In its PM configuration, any spin- and valley-dependent difference in a single ferromagnetic domain can be further enhanced or amplified by the superlattice structure as a result of cascaded modulation, while in its AM configuration, as shown in Fig. 1(c), a different order of band alignment is observed even

for two adjacent ferromagnetic domains, resulting in some spin- and valley-dependent responses that are different from those for a PM configuration.

To show the above physics more clearly, Fig. 2 has schematically depicted the contour plots of spin- and valley-resolved T as a function of θ and Δ_Z , with $d_L = d_R = L = W$. Remarkably, for the PM configuration (top panels), a different T pattern can be observed for different spinor states due to the fully broken spin-valley degeneracy within FMEs. Specifically, as shown in Figs. 2(a) and 2(b) for the K valley, transport for the spin-up state is allowed for a much broader angular space and stronger field modulation compared to those for the spin-down state. The reason is that with considered modulations, the bottom of $E_{K,\downarrow}$ in the FME is higher than other counterparts, while that for $E_{K,\uparrow}$ is lower than the others. This discrepancy further leads to a spin-dependent threshold field modulation (see the white solid and dotted lines), beyond which T is fully prohibited in the whole forward space due to the strong suppression induced by the imaginary k_x in the ferromagnetic domain. Below this threshold modulation, the anisotropy T with visible oscillation could be observed. Similarly, as shown in Figs. 2(c) and 2(d) for the K' valley, spin splitting beneath the FMEs results in a lower branch for the spin-down state and a higher branch for the spin-up state. This makes the pronounced T of the spin-down state accessible for a larger field modulation, in contrast to the observations for the K valley. Very interestingly, except for $T_{K,\uparrow}^{\uparrow\uparrow}$, with respect to normal transport, near perfect transmission with less oscillation can be easily traced for the rest of the spinor states in a broad angular space, e.g., $-0.15\pi \sim 0.15\pi$ for $T_{K',\uparrow}^{\uparrow\uparrow}$ while $-0.1\pi \sim 0.1\pi$ for $T_{K',\downarrow}^{\uparrow\uparrow}$. Importantly, under the Δ_Z modulation, there is a visible window with the allowed transport only for one spinor state, while a prohibited version is for the others, making the perfect spin- and valley-polarized transport expectable.

However, for the AM configuration (bottom panels of Fig. 2), the magnetization reversal of FME2 changes the local order of the underlying bands, forming only two types of T patterns and making the pattern different from that for the PM configuration, even with $\Delta_Z = 0$. For the K valley [see Fig. 1(c)], the up-shifting spin-up band enhances the confinement for the transport of the spin-up state, while the down-shifting spin-down band relaxes the confinement for the transport of the spin-down state. This opposite shift makes the transport of the spin-up (-down) state be limited by the domain beneath the FME2 (FME1). As shown in Figs. 2(e) and 2(f), the T pattern for the spin-up state can be observed for a larger field modulation and broader angular space. Indeed, due to the relations $E_{K',\uparrow}(-M) = E_{K,\downarrow}(M)$ and $E_{K',\downarrow}(-M) = E_{K,\uparrow}(M)$, spin transport for the K' valley is exactly opposite to those for the K valley [see Figs. 2(g) and 2(h)]. Thus, for the AP configuration, the T pattern for the spin-up (-down) state at the K valley is exactly the same as that for the spin-down (-up) state at the K' valley. Due to this feature, any spin- and valley-polarized transport is unexpected for the considered symmetrical structure. Physically, as depicted in Fig. 1(c), although four spinor-resolved bands are well conserved for each ferromagnetic domain, any difference in the spin- and valley-dependent T induced by the first ferromagnetic domain of the periodic unit would be fully compensated by the latter

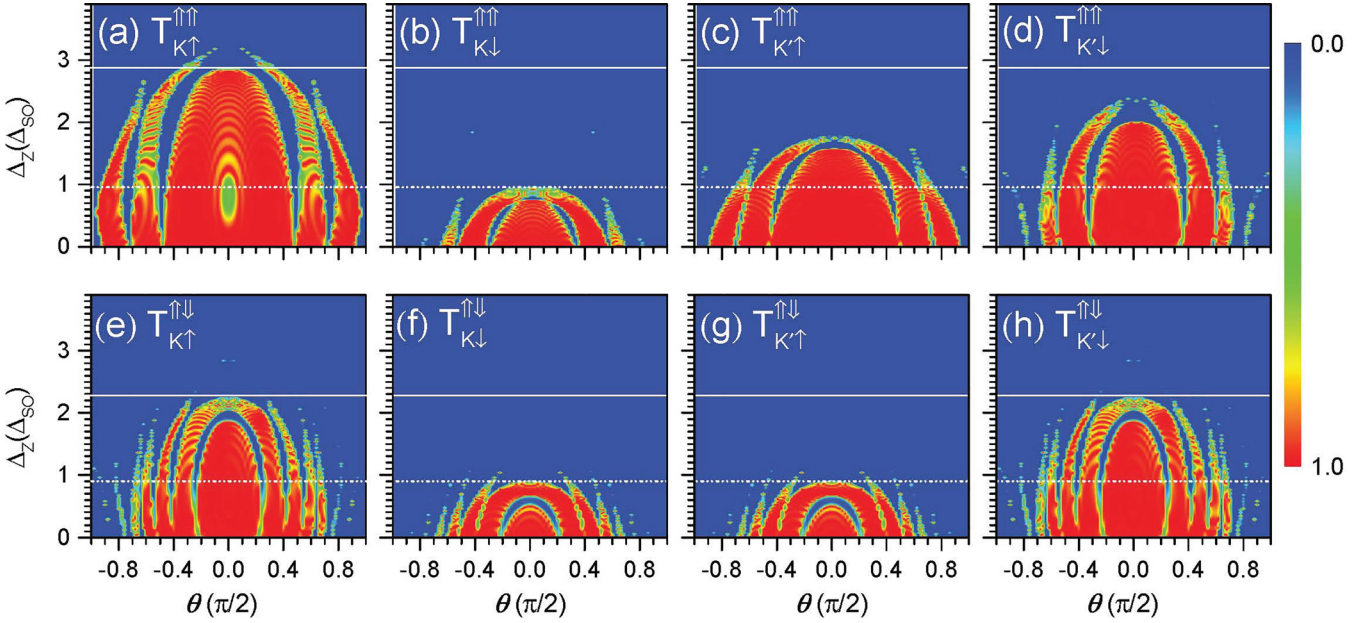


FIG. 2. The contour plots of spin- and valley-dependent transmission probability (T) as a function of θ and Δ_Z for PM (top panels) and AM (bottom panels) configurations with $d_L = d_R = L = W$.

counterpart, naturally leading to zero spin and valley polarization. Indeed, compared to the PM configuration, for each spinor state, the T pattern for the AM configuration has a smaller threshold field modulation, enhanced T oscillation, and much narrower zone for perfect transmission, all of which are highly favorable to observe the configuration-dependent transport properties. Interestingly, for both the PM and AM configurations, due to two types of periodic modulation in our BLS-MSL, much broader perfect transmission and different patterns could be easily observed for all spinor states when compared to those previously reported for monolayer silicene [36]. This implies that better modulation of spin-valley transport is expected for BLS-MSL.

Figure 3(a) shows the corresponding spinor-resolved G as a function of Δ_Z for BLS-MSL in its PM configuration. Generally, with increasing Δ_Z , all G - Δ_Z spectra display a strong oscillatory reduction for Δ_Z lower than a critical one, beyond which the expected G becomes almost zero as a result of the fully prohibited forward transport. For different spinor states, different critical modulations are observed. Concretely, for the shown case, the critical Δ_Z for the K valley has the smallest value for the spin-down state and the highest one for the spin-up state, between which the corresponding values for the K' valley could be traced in a reversal order. Due to these spin- and valley-contrast evolutions, as shown in Fig. 3(b), under the Δ_Z modulation, the pronounced P_S is observable. In particular, for $\Delta_{SO} \leq \Delta_Z < 1.5\Delta_{SO}$, transport for the spin-down state at the K valley has been prohibited, and P_S can be up to 40%, while for $\Delta_Z > 2.4\Delta_{SO}$, perfect spin polarization with $P_S = 100\%$ is explicitly recorded since only the transport of the spin-up state at the K valley is permitted. Symmetrically, once the magnetization direction of all FMEs is fully reversed via some external modulation, perfect spin polarization with $P_S = -100\%$ should also be expected since at that case only the transport for the spin-down state at the K valley is allowed.

As depicted in Fig. 3(c), the corresponding P_V has a different evolution. With increasing Δ_Z , a negative P_V is initially traced with an extreme value of -33% at $\Delta_Z = \Delta_{SO}$ due to the broader perfect transmission for the K' valley. Subsequently, P_V displays an opposite evolution, gradually transforming into a positive value and, finally, being enhanced up to the perfect value for $\Delta_Z > 2.4\Delta_{SO}$. Thus, for the sampled PM configuration, perfect spin and valley polarization could be simultaneously achieved in the symmetric BLS-MSL.

For the comparison, Fig. 4 shows the corresponding results for the AM configuration. Evidently, as can be seen from Fig. 4(a) for the G - Δ_Z spectra, due to the inherent spin-valley locking and antiparallel magnetization alignment, the calculated G - Δ_Z characteristic for the spin-up state at the K

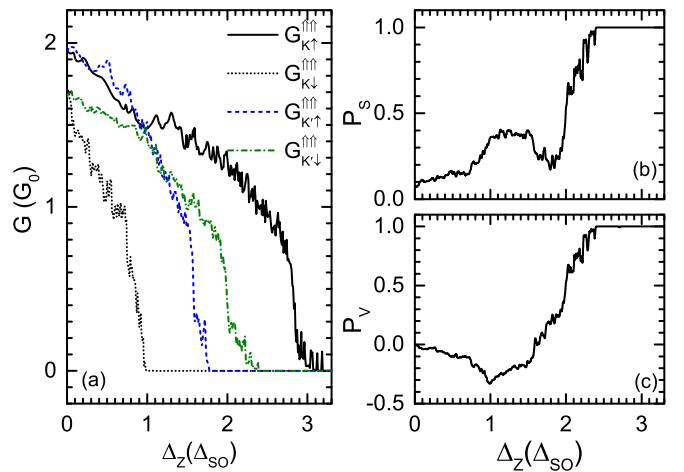


FIG. 3. The (a) spinor-resolved conductance G , (b) spin polarization P_S , and (c) valley polarization P_V as a function of Δ_Z for the symmetric BLS-MSL in its PM configuration with the same parameters as Fig. 2.

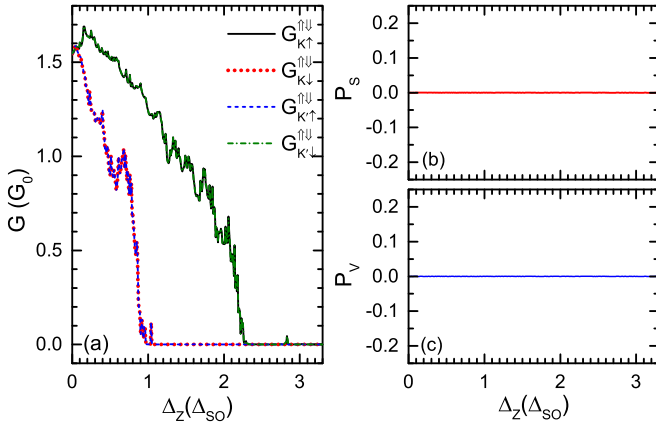


FIG. 4. The (a) spinor-resolved conductance G , (b) spin polarization P_S , and (c) valley polarization P_V as a function of Δ_Z for the symmetric BLS-MSL in its AM configuration with the same parameters as Fig. 2.

valley is completely identical to that for the spin-down state at the K' valley, whereas a different branch is well conserved for the rest of the spinor states. Consequently, as plotted in Figs. 4(b) and 4(c), under the Δ_Z modulation, zero P_S and P_V are well observed. However, comparing to those for the PM configuration, a smaller amplitude can be easily seen for the derived G - Δ_Z spectra. Moreover, for the AM configuration, G almost becomes prohibited for $\Delta_Z > 2.3\Delta_{SO}$, being obviously narrower than that for the PM configuration (see Fig. 3) and further providing an interesting window to achieve the strong contrast in configuration-dependent transport.

Figure 5(a) further presents the corresponding total conductance versus the variation of Δ_Z for both configurations. It is easily observed that with increasing Δ_Z , both $G^{\uparrow\uparrow}$ and $G^{\uparrow\downarrow}$ are reduced with some visible oscillations. For a given Δ_Z , $G^{\uparrow\downarrow}$ has a smaller amplitude while a faster rate than $G^{\uparrow\uparrow}$ due to the compensated modulation within each unit cell. Particularly, as marked by the gray block, once Δ_Z is larger than Δ_{SO} , the discrepancy between $G^{\uparrow\downarrow}$ and $G^{\uparrow\uparrow}$ is suddenly enlarged. This can be attributed to the difference in the number of prohibited spinor states. Specifically, in its AM configuration, transport of both the spin-down state at the K valley and spin-up state at the K' valley becomes prohibited, while for the PM configuration, only the transport of the spin-down state at the K valley is prohibited. Again, as marked by the light-yellow block, once Δ_Z is higher than $2.3\Delta_{SO}$ or so, a new suddenly enhanced difference is observed since the transport of the rest of the spinor states is completely prohibited for the AM configuration, while that for the spin-up state at the K valley is still allowed for the PM configuration. Thus, due to the visible difference in the configuration-dependent conductance, the pronounced m-TMR could be expected.

In Fig. 5(b), the resulting m-TMR is directly depicted as a function of Δ_Z . Evidently, corresponding to the gray-marked region, the calculated m-TMR can be up to 45% or so, while for the higher marked region, the resulting m-TMR could be up to the perfect value. Indeed, within this region, due to the negligible amplitude of $G^{\uparrow\downarrow}$, once the conventional TMR is applied to reflect the difference between $G^{\uparrow\downarrow}$ and $G^{\uparrow\uparrow}$, the calculated TMR for Δ_Z ranging from $2.3\Delta_{SO}$ to $2.8\Delta_{SO}$

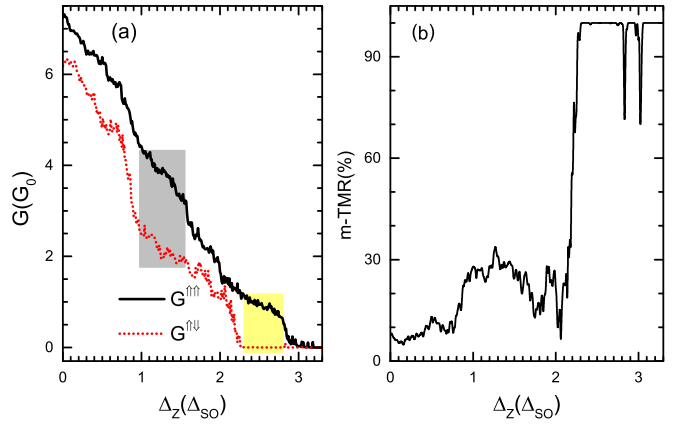


FIG. 5. The (a) configuration-dependent total conductance and (b) corresponding m-TMR as a function of Δ_Z with the same parameters as Fig. 2.

displays rapid oscillation and its value can be up to the order of 10^{16} . Noticeably, as shown in Fig. 1, besides the direct spin-exchange field interaction, due to the spin-valley locking of BLS, the band alignment of magnetic-electric modulated BLS depends not only on the spin, but also on the valley. This enables m-TMR to be indirectly correlated with the valley index, and two valley-contrast oscillations of electronic properties for the same spin state can not only modify the numerical expectation of m-TMR, but also promote its more complex oscillation.

B. BLS-MSL with asymmetric unit cell

As a control case, by breaking the structure symmetry of the unit cell, Fig. 6 depicts the corresponding transport properties for an asymmetric BLS-MSL with $d_L = 21$ nm, $d_R = 14$ nm, $L = 5$ nm, and $W = 10$ nm. As can be seen from

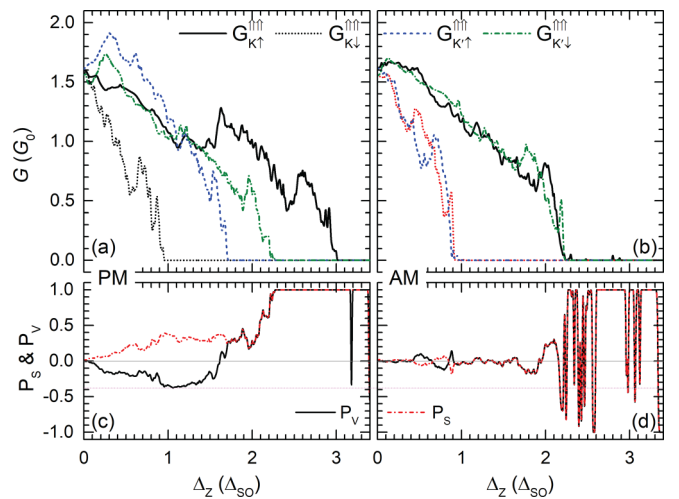


FIG. 6. Transport for the superlattice consisting of the asymmetric unit with $d_L = 21$ nm, $d_R = 14$ nm, $L = 5$ nm, and $W = 10$ nm. In the top panels, spin- and valley-resolved conductance is depicted as a function of Δ_Z for the (a) PM and (b) AM configurations. In the bottom panels, the resulting spin and valley polarization is shown for the (c) PM and (d) AM configurations.

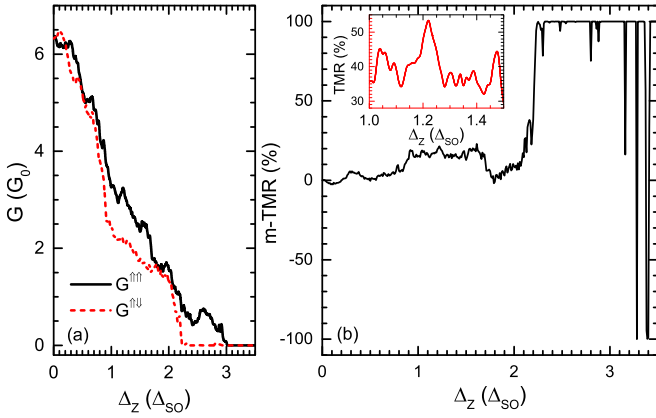


FIG. 7. The (a) configuration-dependent total conductance and (b) corresponding m-TMR as a function of Δ_Z with the same parameters as Fig. 6. In the inset of (b), the enlarged version of the Δ_Z -dependent TMR is further depicted for Δ_Z/Δ_{SO} ranging from 1.0 to 1.5.

Fig. 6(a) for the PM configuration, although the qualitative evolution is well conserved, some visible differences in the calculated G - Δ_Z spectra can still be observed when compared to those shown in Fig. 3(a). For instance, the critical field triggering the prohibited transport has been slightly shifted towards a lower value and, for the small Δ_Z s, transport for the K valley is suppressed, while that for the K' valley is slightly enhanced. However, as shown in Fig. 6(b) for the AM configuration, unlike that for the symmetric unit [Fig. 4(a)], four spinor-resolved G - Δ_Z spectra can still be traced for the structure consisting of asymmetric units. Physically, due to the difference in widths, any spin- and valley-dependent difference induced by the first ferromagnetic domain cannot be fully compensated by the subsequent ferromagnetic domain; therefore, each asymmetric unit plays the same role as a single ferromagnetic domain. Consequently, as shown in the bottom panels, both nonzero P_S and P_V , even for the perfect value, can be expected not only for the PM configuration [Fig. 6(c)], but also for the AM configuration [Fig. 6(d)]. Moreover, as shown in Fig. 6(d), due to the still invisible spinor-dependent resonant tunneling transport in the considered structure, multiple reversals of perfect spin and valley polarization could be recorded for Δ_Z ranging from $2.1\Delta_{SO}$ to $3.2\Delta_{SO}$. This field-controllable switching of spin and valley polarization is very beneficial for the spin-valleytronic applications. Indeed, by elaborately designing the structure of the asymmetric unit cell, the observed polarization switching should also be compatible with the pronounced G .

In Fig. 7, the corresponding configuration-relying total conductance [Fig. 7(a)] and m-TMR [Fig. 7(b)] are depicted as a function of Δ_Z . Obviously, compared to the results shown in Fig. 5(a), the application of the asymmetric unit gives rise to the weaker conductance oscillation [40], smaller discrepancy between the configuration-dependent conductances, and, at some Δ_Z , $G^{\uparrow\downarrow}$ can be larger than $G^{\uparrow\uparrow}$. Consequently, as shown in Fig. 7(b), even a negative m-TMR could be viewed. Due to the smaller difference in the configuration-dependent conductance, with increasing Δ_Z , a relatively smaller m-TMR can be observed initially. For instance, for Δ_Z slightly higher

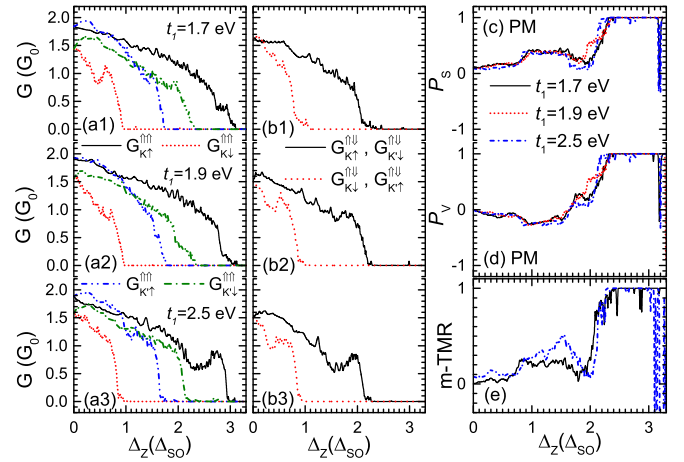


FIG. 8. The spinor-resolved G as a function of Δ_Z for BLS-MSL in its (a1)–(a3) PM and (b1)–(b3) AM configurations with the shown t_1 , where other parameters are the same as Fig. 2. The resulting (c) P_S and (d) P_V for the PM configuration and (e) m-TMR are further depicted as a function of Δ_Z .

than $0.9\Delta_{SO}$, when transport of the spin-down state at the K valley and spin-up state at the K' valley are greatly suppressed for the AM configuration, the expected m-TMR is only 20% or less. Actually, even for the conventional TMR, as shown in the top inset of Fig. 7(b), the highest TMR within these regions can only be up to 50%. Again for Δ_Z larger than $2.2\Delta_{SO}$, transport of all spinor states has been suppressed for the AM configuration, while that for the spin-up state at the K valley still has a visible amplitude, and the expected m-TMR could still be up to 100% with more visible dips. Within this region, once the conventional TMR is applied, a strong oscillation can also be traced with the amplitude of the order of 10^{15} . Thus, by breaking the structure symmetry of the unit cell, near perfect spin polarization, valley polarization, and TMR could be simultaneously achieved for BLS-MSL in its AM configuration.

C. Vertical interlayer coupling and size effect

Under the gate-field modulation, t_1 might be modified due to the field-induced charge redistribution. Figure 8 depicts the Δ_Z -dependent transport properties for different t_1 . With increasing t_1 , for both PM (left panels) and AM (middle panels) configurations, the oscillating spectra for each spinor state shows some visible variations, e.g., suppressing the G peak at $\Delta_Z/\Delta_{SO} = 0.6$ for $G_{K,\downarrow}^{\uparrow\uparrow}$, promoting the formation of a new G peak at $\Delta_Z/\Delta_{SO} = 2.8$ for $G_{K,\uparrow}^{\uparrow\uparrow}$, and sharpening the transition of the spectra near the threshold Δ_Z . However, the emerging order of spinor-resolved threshold modulation is still invariant. Consequently, as shown in the right panels [Figs. 8(c)–8(e)], the resulting P_S , P_V , and m-TMR are very similar to those for $t_1 = 2.025$ eV, but a stronger t_1 is beneficial for the formation of steps for P_S (P_V) but a sharp peak for m-TMR and shifts the perfect polarization region towards lower Δ_Z . At $\Delta_Z/\Delta_{SO} = 1.5$, m-TMR could be enhanced from 25% for $t_1 = 1.7$ eV up to 50% for $t_1 = 2.5$ eV. Thus, a larger t_1 would be favorable to tailor the spin-valley transport in BLS-MSL.

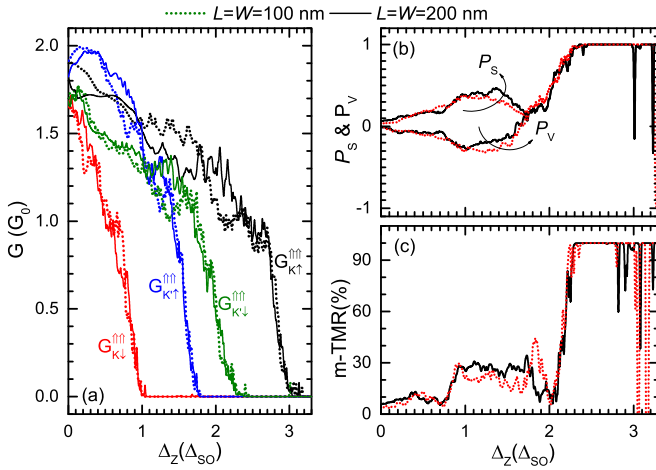


FIG. 9. The (a) spinor-resolved conductance and (b) spin (valley) polarization P_S (P_V) as a function of Δ_Z for BLS-MSL in its PM configuration with $L = W = 100$ nm (dotted line) and 200 nm (solid line), while $d_L = d_R = 12.5$ nm. (c) The corresponding m-TMR depicted as a function of Δ_Z .

To examine the effect of structure parameters on the observed features, still with $d_L = d_R = 12.5$ nm and taking $L = W = 100$ ($= 200$) nm, Fig. 9(a) plots the G - Δ_Z spectra for BLS-MSL in its PM configuration. Evidently, changing the structure parameters can actually modify the pattern of oscillatory G for all spinor states, most strikingly for the spin-up state at the K valley, but the whole field-engineered evolution is still very similar to those shown above, almost showing the same prohibited region ($G = 0$) for the spinor state. The reason is that $L(W)$ is mainly responsible for the propagating phase $e^{\pm ik_w L(W)}$ in the NM domains, forming more Fabry-Perot-like quasibound states for a larger $L(W)$ and thus changing the G pattern. Consequently, as shown in Figs. 9(b) and 9(c), besides the small numerical difference and additional dips, the calculated P_S , P_V , and m-TMR are highly similar to those shown in Fig. 3. Importantly, perfect spin and valley polarization with $P_S = P_V = 100\%$ can still be traced for $\Delta_Z/\Delta_{SO} = 2.4 \sim 2.8$, for which only the pronounced transport of the spin-up state at the K valley is permitted. The new formed dips indicate that some suppressed G peaks that are unseen in the linear scale of Fig. 9(a) should be expected in the prohibited region due to resonant tunneling transport relating to quasibound states. Indeed, we have also reproduced the calculations for other d_L and d_R , where similar features are preserved, implying the above shown features are less impacted by size parameters.

To show the necessity of dual-fold periodic modulation, Fig. 10 depicts the G - Δ_Z spectra of a monolayer silicene magnetic superlattice by applying our model potential (solid line) and that reported in Ref. [36] (dotted line) with $W = L = d_L = d_R = 179.2$ nm. Obviously, for both PM [Fig. 10(a)] and AM [Fig. 10(b)] configurations, our calculations reasonably reproduce the G - Δ_Z spectra of Ref. [36] for $M = 0.6\Delta_{SO}$. However, once our model potential is applied, for both configurations, much stronger oscillation could be observed due to the enhanced modulations, showing sharp peaks and a broad valley. Meanwhile, in its PM configuration, the

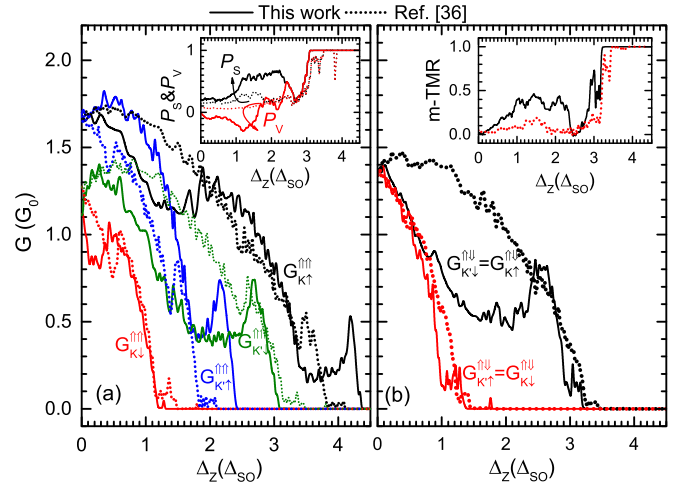


FIG. 10. The spinor-resolved G as a function of Δ_Z for a monolayer silicene magnetic superlattice in its (a) PM and (b) AM configurations by taking the same parameters as Ref. [36] for $M = 0.6\Delta_{SO}$: the solid line is for our model potential, while the dotted line is for Ref. [36]. In the insets of (a) and (b), the resulting evolution of P_S (P_V) for the PM configuration and m-TMR are, respectively, shown as a function of Δ_Z .

prohibited conductance region has been shifted towards higher Δ_Z for the spin-up state, while slightly lower Δ_Z for the spin-down state. Owing to this oppositely spin-dependent shift, as shown in the inset of Fig. 10(a), an enhanced P_S and P_V with a broader Δ_Z window for perfect polarization can be traced. Most importantly, as shown in the inset of Fig. 10(b), although a similar evolution of m-TMR is observed for both model potentials, remarkable enhancement of m-TMR and a broadening perfect plateau should be expected for our dual-fold periodic potential. These observations fully indicate the advantages of dual-fold periodic modulation in tailoring the spin-valley transport of BLS for logic applications.

So far, only with a specific set of parameters have the the field-tailorable spin polarization, valley polarization, and m-TMR been theoretically demonstrated to be accessible in BLS-MSL without the prerequisite single-valley approximation, but the shown physics can also be generalized to other sets of parameters. For instance, with a different E , the same physics promises a similar observation besides the variation of critical Δ_Z to turn the transport of a specific spinor state, while for a much stronger exchange field, a broader window is expected for the observation of perfectly spin and valley-polarized transport in BLS-MSL. Thus, it is convincing that near perfect spin polarization, valley polarization, and colossal tunneling magnetoresistance could be efficiently engineered by a perpendicular gate field in BLS-MSL. Most importantly, by reversing the direction of either the electric field or exchange field, different local band alignments of BLS-MSL enable the highly selective region only for one spinor state to be transferred from the spin-up state at the K valley into the other spinor state, further creating a perfect switch of spin and/or valley polarization for spin-/valley-logic applications.

IV. CONCLUSIONS

By locally making the bilayer silicene ferromagnetic via magnetic proximity mechanism, we have theoretically investigated the ballistic spin and valley-resolved transport in a ferromagnetic bilayer silicene superlattice, for which a periodic unit cell is composed of two cascaded ferromagnetic-nonmagnetic pairs. Following the formulated four-band scattering matrix method, it is demonstrated for the superlattice with a symmetric unit cell that perfect spin polarization and valley polarization could be efficiently engineered by the field modulation once two neighboring ferromagnetic domains show a parallel magnetization alignment, while by only switching the magnetization alignment of neighboring ferromagnetic domains from a parallel configuration into an antiparallel one, a field-independent yet unpolarized scenario is expected for the same structure. Importantly, between two magnetization configurations, the pronounced difference in the configuration-dependent conductance could be observed, especially at the region with a pronounced value for a

parallel magnetization configuration and a negligible one for an antiparallel magnetization configuration; perfect m-TMR or colossal TMR of the order of 10^{16} is observed for the ferromagnetic superlattice.

With an asymmetric unit cell, it is also observed for the formed magnetic superlattice that even in its antiparallel magnetization configuration, near perfect spin polarization, valley polarization, and strong TMR can still be efficiently engineered by the gate field. This field-controllable feature indicates that the magnetic superlattice might be a potential strategy to develop spin- and valleytronic applications residing on bilayer silicene.

ACKNOWLEDGMENTS

This work was financially supported by the National Natural Science Foundations of China through Grants No. 11464024, No. 62274078 and the Yunnan Ten-Thousand Talents Plan Yong & Elite Talents Project under Grant No. YNWR-QNBJ-2018-226.

-
- [1] P. Vogt, P. De Padova, C. Quaresima, J. Aila, E. Frantzeskakis, M. C. Asensio, A. Resta, B. Ealet, and G. Le Lay, Silicene: Compelling experimental evidence for graphenelike two-dimensional silicon, *Phys. Rev. Lett.* **108**, 155501 (2012).
- [2] A. Fleurence, R. Friedlein, T. Ozake, H. Kawai, Y. Wang, and T. Yamada-Takamura, Experimental evidence for epitaxial silicene on diboride thin films, *Phys. Rev. Lett.* **108**, 245501 (2012).
- [3] L. Meng, Y. Wang, L. Zhang, S. Du, R. Wu, L. Li, Y. Zhang, G. Li, H. Zhou, W. A. Hofer, and H. J. Gao, Buckled Silicene Formation on Ir(111), *Nano Lett.* **13**, 685 (2013).
- [4] B. J. Feng, Z. Ding, S. Meng, Y. G. Yao, X. Y. He, P. Cheng, L. Chen, and K. H. Wu, Evidence of silicene in honeycomb structures of silicon on Ag(111), *Nano Lett.* **12**, 3507 (2012).
- [5] P. De Padova, P. Vogt, A. Resta, J. Avila, I. Razado-Colambo, C. Quaresimal, C. Ottaviani, B. Olivieri, T. Bruhn, T. Hirahara, T. Shirai, S. Hasegawa, M. C. Asensio, and G. Le Lay, Evidence of Dirac fermions in multilayer silicene, *Appl. Phys. Lett.* **102**, 163106 (2013).
- [6] P. Vogt, P. Capiod, M. Berthe, A. Resta, P. De Padova, T. Bruhn, G. Le Lay, and B. Grandidier, Synthesis and electrical conductivity of multilayer silicene, *Appl. Phys. Lett.* **104**, 021602 (2014).
- [7] P. De Padova, A. Generosi, B. Paci, C. Ottaviani, C. Quaresima, B. Olivieri, E. Salomon, T. Angot, and G. Le Lay, Multilayer silicene: Clear evidence, *2D Mater.* **3**, 031011 (2016).
- [8] R. Yaokawa, T. Ohsuna, T. Morishita, Y. Hayasaka, M. J. S. Spencer, and H. Nakano, Monolayer-to-bilayer transformation of silicenes and their structural analysis, *Nat. Commun.* **7**, 10657 (2016).
- [9] J. J. Zhao, H. Liu, Z. Yu, R. Quhe, S. Zhou, Y. Wang, C. C. Liu, H. Zhong, and N. Han, Rise of silicene: A competitive 2D material, *Prog. Mater. Sci.* **83**, 24 (2016).
- [10] P. De Padova, C. Ottaviani, C. Quaresima, B. Olivieri, P. Imperatori, E. Salomon, T. Angot, L. Quagliano, C. Romano, A. Vona, M. Muniz-miranda, A. Generosi, B. Paci, and G. Le Lay, 24 h stability of thick multilayer silicene in air, *2D Mater.* **1**, 021003 (2014).
- [11] L. Tao, E. Cinquanta, D. Chiappe, C. Grazianetti, M. Fanciulli, M. Dubey, A. Molle, and D. Akinwande, Silicene field-effect transistors operating at room temperature, *Nat. Nanotechnol.* **10**, 227 (2015).
- [12] M. Ezawa, Quasi-topological insulator and trigonal warping in gated bilayer silicene, *J. Phys. Soc. Jpn.* **81**, 104713 (2012).
- [13] F. Liu, C. C. Liu, K. H. Wu, F. Yang, and Y. G. Yao, $d+id'$ chiral superconductivity in bilayer silicene, *Phys. Rev. Lett.* **111**, 066804 (2013).
- [14] J. J. Liu and W. G. Zhang, Bilayer silicene with an electrically tunable wide band gap, *RSC Adv.* **3**, 21943 (2013).
- [15] B. Huang, H. X. Deng, H. Lee, M. Yoon, B. G. Sumpter, F. Liu, S. C. Simth, and S. H. Wei, Exceptional optoelectronic properties of hydrogenated bilayer silicene, *Phys. Rev. X* **4**, 021029 (2014).
- [16] J. E. Padiha and R. B. Pontes, Free-standing bilayer silicene: The effect of stacking order on the structural, electronic, and transport properties, *J. Phys. Chem. C* **119**, 3818 (2015).
- [17] H. X. Fu, J. Zhang, Z. J. Ding, H. Li, and S. Meng, Stacking dependent electronic structure of bilayer silicene, *Appl. Phys. Lett.* **104**, 131904 (2014).
- [18] T. N. Do, P. H. Shih, G. Gumbs, D. H. Huang, C. W. Chiu, and M. F. Lin, Diverse magnetic quantization in bilayer silicene, *Phys. Rev. B* **97**, 125416 (2018).
- [19] T. N. Do, G. Gumbs, P. H. Shih, D. H. Huang, and M. F. Lin, Valley- and spin-dependent quantum Hall states in bilayer silicene, *Phys. Rev. B* **100**, 155403 (2019).
- [20] K. Jatiyanon and B. Soodchomshom, Spin-valley and layer polarizations induced by topological phase transitions in bilayer silicene, *Superlatt. Microstruct.* **120**, 540 (2018).
- [21] M.-M. Zhang, L. Xu, and J. Zhang, Topological insulator state in gated bilayer silicene, *J. Phys.: Condens. Matter* **27**, 445301 (2015).

- [22] G. Q. Xiong, D. J. Wang, F. J. Xu, Y. X. Ma, T. T. Wei, X. Li, and Y. Wang, Spin-valley polarized transport in a field-controllable bilayer silicene superlattice, *Phys. Rev. B* **106**, 205409 (2022).
- [23] X. F. Ouyang, Z. Y. Song, and Y. Z. Zhang, Fully spin-polarized current in gated bilayer silicene, *Phys. Rev. B* **98**, 075435 (2018).
- [24] H. Haugen, D. Huertas-Hernando, and A. Brataas, Spin transport in proximity-induced ferromagnetic graphene, *Phys. Rev. B* **77**, 115406 (2008).
- [25] Y. Wu, G. Yin, L. Pan, A. J. Grutter, Q. J. Pan, A. L. Lee, D. A. Gilbert, J. A. Borchers, W. Ratcliff, A. Li, X. D. Han, and K. L. Wang, Large exchange splitting in monolayer graphene magnetized by an antiferromagnet, *Nat. Electron.* **3**, 604 (2020).
- [26] P. Wei, S. W. Lee, F. Lemaitre, D. Cutaia, W. J. Cha, F. Katmis, Y. Zhu, D. Heiman, J. Hone, J. S. Moodera, and C. T. Chen, Strong interfacial exchange field in the graphene/EuS heterostructure, *Nat. Mater.* **15**, 711 (2016).
- [27] T. Yokoyama, Controllable valley and spin transport in ferromagnetic silicene junctions, *Phys. Rev. B* **87**, 241409(R) (2013).
- [28] Y. Wang, Resonant spin and valley polarization in ferromagnetic silicene quantum well, *Appl. Phys. Lett.* **104**, 032105 (2014).
- [29] R. Saxena, A. Saha, and S. Rao, Conductance, valley and spin polarizations, and tunneling magnetoresistance in ferromagnetic-normal-ferromagnetic junctions of silicene, *Phys. Rev. B* **92**, 245412 (2015).
- [30] V. Vargiamidis and P. Vasilopoulos, Electric- and exchange-field controlled transport through silicene barriers: Conductance gap and near-perfect spin polarization, *Appl. Phys. Lett.* **105**, 223105 (2014).
- [31] D. L. Wang, Z. Y. Huang, Y. Y. Zhang, and G. J. Jin, Spin-valley filter and tunnel magnetoresistance in asymmetrical silicene magnetic tunnel junctions, *Phys. Rev. B* **93**, 195425 (2016).
- [32] N. Missault, P. Vasilopoulos, V. Vargiamidis, F. M. Peeters, and B. Van Duppen, Spin- and valley-dependent transport through arrays of ferromagnetic silicene junctions, *Phys. Rev. B* **92**, 195423 (2015).
- [33] N. Missault, P. Vasilopoulos, F. M. Peeters, and B. Van Duppen, Spin- and valley-dependent miniband structure and transport in silicene superlattices, *Phys. Rev. B* **93**, 125425 (2016).
- [34] Q. T. Zhang, K. S. Chan, and J. B. Li, Electrically controllable sudden reversals in spin and valley polarization in silicene, *Sci. Rep.* **6**, 33701 (2016).
- [35] Z. Rashidian, Y. Hajati, S. Rezaei-pour, and S. Baher, Controllable spin and valley polarized current through a superlattice of normal/ferromagnetic/normal silicene junction, *Phys. E* **86**, 111 (2017).
- [36] J. G. Rojas-Briseño, M. A. Flores-Carranza, P. Villasana-Mercado, S. Molina-Valdovinos, and I. Rodríguez-Vargas, Tunneling magnetoresistance and spin-valley polarization in magnetic silicene superlattices, *Phys. Rev. B* **103**, 155431 (2021).
- [37] Z. P. Niu, Y. M. Zhang, and S. Dong, Enhanced valley-resolved thermoelectric transport in a magnetic silicene superlattice, *New J. Phys.* **17**, 073026 (2015).
- [38] B. Van Duppen and F. M. Peeters, Four band tunneling in bilayer graphene, *Phys. Rev. B* **87**, 205427 (2013).
- [39] I. Snyman and C. W. J. Beenakker, Ballistic transmission through a graphene bilayer, *Phys. Rev. B* **75**, 045322 (2007).
- [40] O. Oubram, J. G. Rojas-Briseño, S. Molina-Valdovinos, and I. Rodríguez-Vargas, Improvement of tunneling magnetoresistance and spin-valley polarization in magnetic silicene superlattices induced by structural disorder, *Phys. Rev. B* **105**, 115408 (2022).